ACS NANO

www.acsnano.org

ARTICLE

Sculpting Enzyme-Generated Giant Polymer Brushes

Jessica L. Faubel, Wenbin Wei, and Jennifer E. Curtis*

Cite This: *ACS Nano* 2021, 15, 4268–4276

Read Online

ACCESS | Metrics & More | Article Recommendations | Supporting Information

ABSTRACT: We present a simple yet versatile method for sculpting ultra-thick, enzyme-generated hyaluronan polymer brushes with light. The patterning mechanism is indirect, driven by reactive oxygen species created by photochemical interactions with the underlying substrate. The reactive oxygen species disrupt the enzyme hyaluronan synthase, which acts as the growth engine and anchor of the end-grafted polymers. Spatial control over the grafting density is achieved through inactivation of the enzyme in an energy density dose-dependent manner, before or after polymerization of the brush. Quantitative variation of the brush height is possible using visible wavelengths and illustrated by the creation of a brush gradient ranging from 0 to 6 μm in height over a length of 56 μm (approximately a 90 nm height increase per micron). Building upon the fundamental insights presented in this study, this work lays the foundation for the flexible and quantitative sculpting of complex three-dimensional landscapes in enzyme-generated hyaluronan brushes.

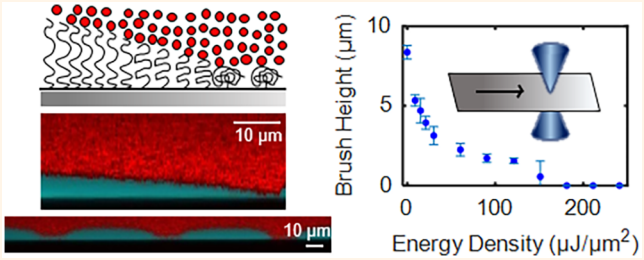

KEYWORDS: *polymer brush, hyaluronan, enzyme, gradient, topography, photopattern, reactive oxygen species*

Three-dimensional nanostructured polymer brushes are finding increasing applications in materials science, chemistry, and the biosciences.[1−6] Polymer brush gradients and other topographies have been used in combinatorial studies of a broad range of physiochemical phenomena,[7−12] enable the directed transport of soft materials like nanoparticles and cells,[13,14] facilitate the screening of design strategies for protein and cell−substrate interactions,[15,16] and are useful tools in expediently exploring the fundamental behavior of the brushes.[5,9,10,17] Sculpted brushes can also be used to tune the local environment (*e.g.*, porosity, stiffness, roughness)[11,18] or orchestrate the organization of complex materials such as structured nanoparticle-polymer film composites.[19−21]

Various strategies exist to sculpt polymer brushes, typically by spatially varying the grafting density[22−26] or the molecular weight.[8,27−29] Generally, brush topography can be programmed through controlled placement of the polymer initiators *via* lithographic techniques or the availability of monomers.[30−34] Another strategy involves varying the feature density—the spacing of discrete, constant density nanobrushes—in order to achieve impressively complex architectures.[35] One commonality of all these examples, however, is that the sculpted brushes are almost always less than a few hundred nanometers thick.

Ultra-thick three-dimensional polymer brushes present many advantages especially in domains where brush gradients or more complex topography are desirable. Micron-sized brushes provide a larger dynamic range for height manipulation and associated properties like porosity and stiffness. The increased degree of polymerization inherently provides more volume for uptake of molecules and a greater number of binding sites to bind, organize, or sort molecules and particles, for example, in separations applications.[36,37] For applications dependent on nonlinear topographies, larger brushes offer a thicker template on which to execute complex patterns. Microns-thick polymer brushes also have the unusual advantage of being directly characterizable using optical microscopy (Figure 1), potentially diversifying design possibilities and read out for various applications.

Here, we introduce a strategy to sculpt ultra-thick, enzyme-generated polymer brushes. As a member of a growing class of polymer brushes and films fabricated by enzymes,[38−40] the focus of this work is a microns-thick polymer brush assembly composed of the polyelectrolyte hyaluronic acid (HA), generated by the enzyme hyaluronan synthase. HA synthase can generate polymers up to 25 μm (10 MDa) so that the

Received: August 16, 2020
Accepted: February 16, 2021
Published: February 22, 2021

https://dx.doi.org/10.1021/acsnano.0c06882
ACS Nano 2021, 15, 4268–4276

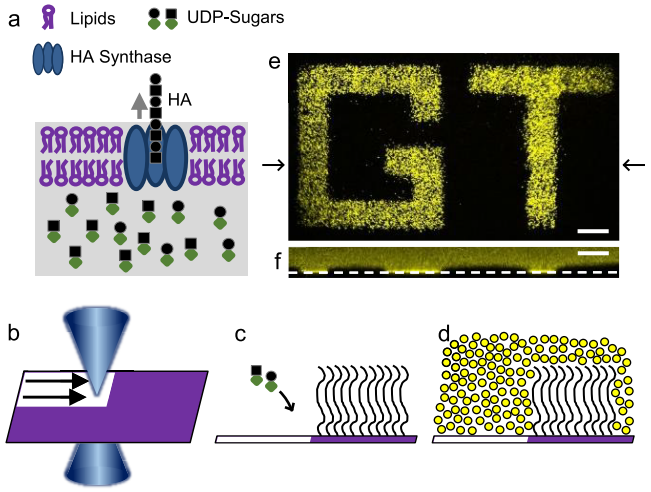

Figure 1. (a) Schematic of the transmembrane HA synthase enzyme processively synthesizing HA by alternating addition of the sugar components (UDP are green, and sugars are black). (b) Schematic of laser treatment of the enzyme-rich (purple) surface. White areas indicate phototreated areas. (c) After photopatterning, components necessary for enzymatic synthesis of the HA are added, and HA is generated in unirradiated regions. (d) Fluorescent 200 nm particles are excluded from areas with the brush present and allowed to fill in gaps where the brush is absent which allows for visualization of the pattern. (e) Binary patterning in the form of a GT (*i.e.*, Georgia Institute of Technology). Top down (*XY*) confocal microscope view at the glass interface. 200 nm beads (false colored yellow) appear in areas without the brush. Black regions are where the brush is present. t_{growth} = 16 h. (f) Side (*XZ*) confocal microscope view across the middle of the top image, as indicated by the black arrows. The glass interface is labeled with a white dotted line. Scale bars are 20 μm.

brush height can be tuned from a few hundred nanometers to tens of microns by adjusting polymerization time, ionic strength, or solvent.[40,41] However, sculpting the giant brush by spatially modifying the grafting density or varying the molecular weight is nontrivial. This is because in order to harness the impressive capabilities of HA synthase, we must stabilize this lipid-dependent transmembrane protein in its natural membrane environment.[42] This is achieved by collecting fragments of membrane from bacteria which have been genetically manipulated to overexpress the HA synthase enzyme. The membrane fragments contain dense configurations of active HA synthase. HA brushes are then fabricated by decorating a substrate with the membrane fragments and initiating polymerization by providing the prerequisite sugar monomers (Figure 1a). This explains why traditional lithographic patterning of grafting density is difficult, as the grafting density is governed by the HA synthase expression levels in the bacterial membrane fragments.

In this work, we investigate whether visible light can be used to alter HA synthase function and hence modify the underlying grafting density of the enzyme-generated brushes for the controlled sculpting of structured three-dimensional brushes. Simple experiments establish that quantitative changes in brush height can be achieved by varying laser intensity, exposure time, or wavelength. We demonstrate how this insight enables brush sculpting by creating an ultra-thick linear brush gradient with a height increase of 90 nm per micron from 0 to 6 microns. We then delve into determining the mechanism of the brush height patterning by implementing a series of experiments based on our understanding of how visible light interacts with hyaluronan, lipids, and proteins. Integrating the knowledge gained by comparing patterning results before and after brush growth and in the presence and absence of bacterial membrane fragments, we provide strong evidence that reactive oxygen species (ROS), generated by light-membrane fragment interactions, are the agent by which HA synthase function is destroyed.

RESULTS AND DISCUSSION

We explored the potential for photopatterning the HA brush with a 405 nm laser motivated by the idea that near UV or blue light might damage proteins and thus provide a way to manipulate the HA synthase and hence the brush's grafting density. Testing this hypothesis with a laser scanning confocal microscope was straightforward because it inherently enables photomicropatterning, variation of intensity, exposure time, and wavelength. We started by prepatterning the HA synthase substrates with no brush (Figure 1b). The confocal's 405 nm laser was focused on the surface and raster scanned in a selected region at fixed power. Upon completion of the laser application, HA synthesis was switched on by adding the two required uridine diphosphate (UDP)-sugar monomers, and then the brush growth was allowed to proceed for t_{growth} = 16 h (Figure 1c). Experimentation established that regions exposed to at least ~200 $\mu J/\mu m^2$ lose the capacity to generate a polymer brush (see Materials and Methods). This energy

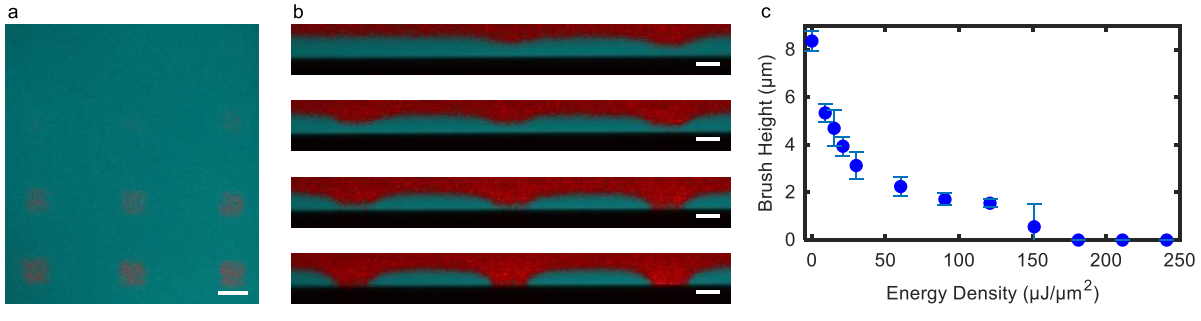

Figure 2. (a) *XY* confocal image of square patterned areas with increasing laser energy density applied, viewed at the surface. Red fluorescent 200 nm particles sit closer and closer to the surface in areas treated with higher energy densities. Cyan colored dextran highlights regions where the brush is present. Scale bar is 20 μm. (b) Average intensity *XZ* side views of each row corresponding with the image in (a). Black is the glass substrate. Scale bars are 10 μm. (c) Energy density of the applied laser *versus* the resulting height of brushes grown for 16 h. N = 3 brushes. λ = 405 nm.

https://dx.doi.org/10.1021/acsnano.0c06882
ACS Nano 2021, 15, 4268−4276

density was achieved by scanning each patterned area five consecutive times at 200 μs/pixel at the desired laser intensity, which could be varied from 0 to 100% ($P_{405,max}$ = 561 μW).

The resulting patterns are readily visualized with the same confocal microscope by implementation of a particle exclusion assay (Figure 1d).[43,44] As demonstrated in previous work,[40] fluorescent nanoparticles of 200 nm are sterically hindered from penetrating the HA brush and thus serve as a means of outlining a brush's upper interface. Figure 1e demonstrates the binary patterning of the brush in a ~200 μm × 100 μm area. In this *XY* view taken at the glass substrate, the 200 nm nanoparticles appear in areas where the 405 nm laser was applied. The laser exposure fully disrupts the HA synthase function, as evidenced by the lack of brush growth. In the untreated sample areas, the brush grew normally, excluding the 200 nm particles.

Next, we explored whether the brush could be tuned to reach intermediate heights with reduced exposures to the 405 nm laser. In a 4 × 3 array, 12 different laser intensities were applied for the same exposure time to square areas (17.4 × 17.4 μm^2). Then, the brush was grown for 16 h, and the height in each patterned region was analyzed. Results from three such experiments are summarized in Figure 2. Figure 2a shows the *XY* view at the glass interface with regions of increasing energy density (left to right, top to bottom). The subsequent decreases in the thickness of the brush are visualized by the increasing amounts of the 200 nm red fluorescent beads present at the glass interface and by the decreasing gap present between the black glass interface and the red nanoparticles in the *XZ* side views in Figure 2b. The energy densities necessary to achieve a range of final brush heights (0–8 μm, t_{growth} = 16 h) are plotted for constant exposure time (405 nm, 5 scans at 200 μs/pixel) and variable laser intensity in Figure 2c.

Notably, distinct brush curvature in the evenly patterned areas likely arises from a polymer splay at the edges of the patterned area.[45,46] The effect is increasingly pronounced in the areas where the brush height is reduced so that more free space is available for the surrounding brush spill over and distort the brush profile. In the future, we will systematically investigate these effects, as they are fundamentally interesting and they will impact any sophisticated sculpting of the brush topography.[46]

With the fine-tuned photomanipulation of the brush height established, one can create more complex brush topographies. To explore this, we designed a brush gradient with a height that linearly increases 6-fold over an extent of ~56 μm (Figure 3). At its highest point, the brush height is 5.8 μm. To create this gradient, the data from Figure 2 were used to determine the necessary energy densities to realize height decreases in one-half micron steps. Small rectangular areas (6.25 μm × 20 μm) were irradiated in nine adjacent regions, as outlined with dashed lines in Figure 3a. After this prepatterning treatment, the brush was grown for 4 h. The resultant brush heights in Figure 3c show that the height decreases in a linear fashion by approximately one-half micron (~590 nm) per 6.25 μm region, corresponding to a ~90 nm change in brush height per lateral micron. Although the patterning is discrete, the final brush appears as a continuous gradient (Figure 3b), an effect resulting from the significant splay arising in thick polymer brushes.

Polymer brush patterning schemes are typically limited to either prepatterning or postpatterning (before or after brush growth), and most are incapable of doing both, especially using

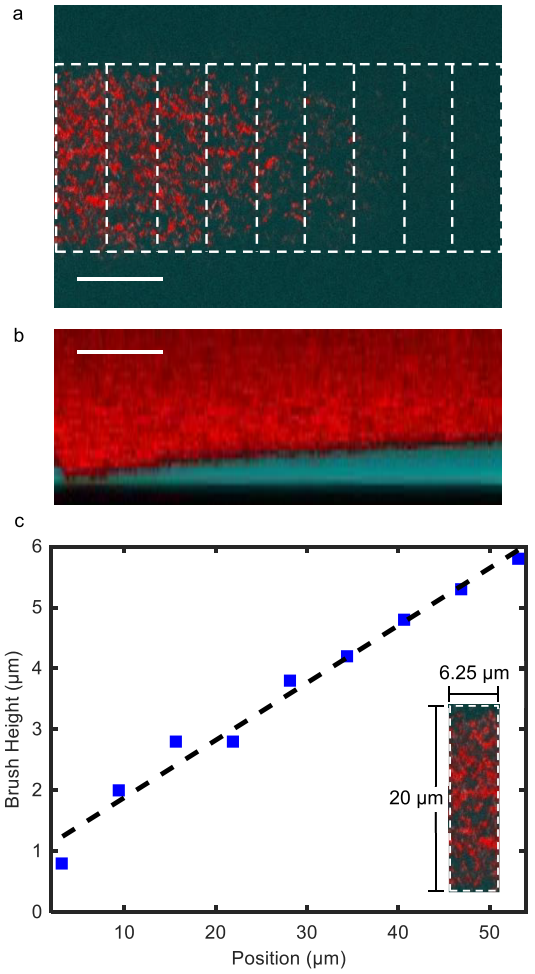

Figure 3. (a) *XY* view at the glass substrate under the brush. The white outlined areas depict the nine regions patterned at preselected energy densities. The brush thickness increases linearly in height to the right. (b) Side view of the linear brush gradient. The maximum height is 5.8 μm. All scale bars are 10 μm. (c) Average height of the brush in each patterned region. N = 1 brush. λ = 405 nm, t_{growth} = 4 h. Black dotted line is a linear fit, H = 0.94 + 0.09x, where x is in microns.

the same method. In Figure 4, we illustrate the capacity to implement both approaches on one sample (see also Figure S2). While this capability was expected since photodisruption of the HA synthase is the hypothesized mechanism, an unforeseen outcome was the nearly overlapping brush heights after pre- and postpatterning at the same energy densities. Below, we will use this result to shed insight on the mechanism behind the brush height photopatterning and use it to address the possible connection to grafting density.

To investigate the mechanism of the photopatterning and to potentially expand the methodology's flexibility, we examined whether longer wavelengths also enable manipulation of brush height. Similar results can be achieved using λ = 488 nm and λ = 635 nm (Figure 5). The efficiency of the patterning is reduced with increasing wavelength, however, requiring higher energy densities. Due to the efficiency of patterning with the 405 nm laser, very little exposure time was required to pattern. Therefore, the only way to achieve a spread of energy densities was to vary the intensity of the laser from 0 to 100% with a set exposure time. With longer wavelengths, the exposure time necessary to eliminate the brush increased significantly. In

https://dx.doi.org/10.1021/acsnano.0c06882
ACS Nano 2021, 15, 4268–4276

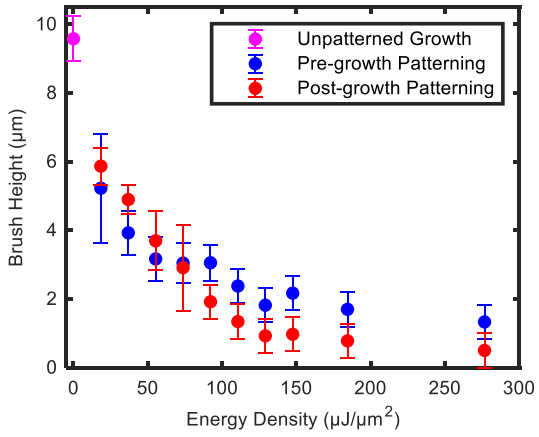

Figure 4. Brush height *versus* energy density measurements for pre- and postpatterning the same brush using identical settings. λ = 405 nm. N = 3 brushes for each data set.

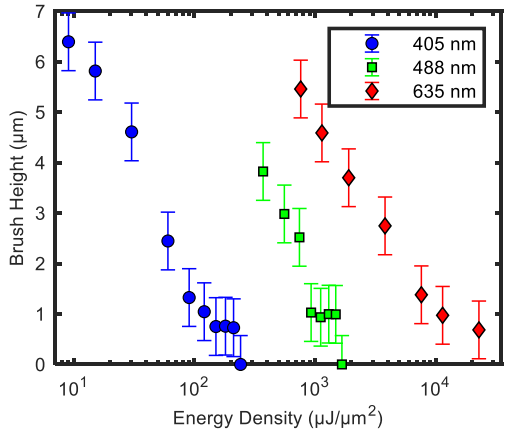

Figure 5. Energy density of the applied laser *versus* the resulting brush height. Blue: t_{growth} = 16 h. λ = 405 nm. N = 3 brushes. Green: t_{growth} = 16 h. λ = 488 nm. N = 1 brush. Red: t_{growth} = 16 h. λ = 635 nm. N = 1 brush.

Figure 5, 488 and 635 nm data represent varied exposure time, rather than varied laser intensity as with the 405 nm.

Future applications of the HA brushes will likely adopt a chemically stabilized version of the brush because they are more amenable to long-term usage. Indeed, the HA brushes studied thus far are inherently unstable, decaying over a few days due to the release of HA from the HA synthase.[40] To resolve this issue, we previously established that a robust chemical attachment to the underlying substrate can be achieved using carbodiimide chemistry to generate an amide bond between the HA's available carboxyl groups and the amines present on the surface due to the polyethylenimine (PEI) film used in the scheme for fragment attachment.[40]

For these chemically stabilized "reinforced" brushes, the grafting density is independent of viable HA synthase, unlike for the "unreinforced" brushes where the HA synthase must both make and anchor the HA. The reinforced brush's independence from HA synthase was previously established by using the surfactant sodium dodecyl sulfate (SDS), which we applied to remove the bacterial membrane fragments. Elimination of the membrane fragments destroyed unreinforced brushes as expected; reinforced brushes remained unchanged.[40] Hence, in the reinforced brush case, the loss of stability or activity in HA synthase due to photopatterning should not affect the final brush height.

Yet, despite this seemingly well-founded prediction, we found that photopatterning the reinforced brushes also enables manipulation of the brush height. Figure 6a,b shows a brush that was grown for 4 h, reinforced, and then successfully patterned with the same exposure settings previously determined to result in no brush growth in a prepatterning scheme. This unexpected result may in fact be the most useful implementation of the patterning method since it is demonstrated to work on stabilized, ultra-thick, HA brushes. Such brushes are ideal for applications, and combining their stability with access to postpatterning enables their fabrication, storage, and future patterning as needed.

To further investigate the mechanism behind the HA brush sculpting, we designed a simple experiment to investigate

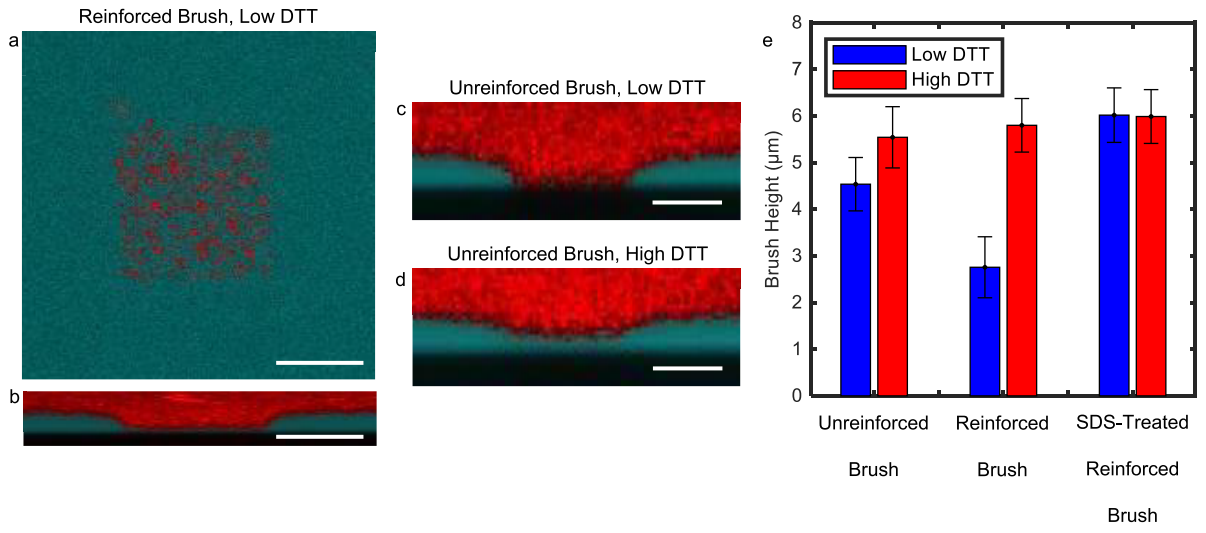

Figure 6. (a) A 4 h growth *reinforced* brush with a square patterned region at the center. (b) *XZ* average side view confirms the brush elimination in patterned region. (c) 5 mM DTT. Average *XZ* side view of a postpatterned 4 h brush shows the full brush removal. (d) 50 mM DTT. Increased DTT significantly reduces the photopatterning efficacy. All scale bars are 10 μm. (e) Height of different brush types *versus* DTT concentration after postpatterning. N = 3 brushes per type, t_{growth} = 4 h. λ = 405 nm, ~280 μJ/μm^2.

https://dx.doi.org/10.1021/acsnano.0c06882
ACS Nano 2021, 15, 4268−4276

Table 1. Summary of the Patterning Mechanism for Each Brush Type and the Evidence from Each Type of Experiment That Supports These Conclusions

Summary of Patterning Mechanism by Brush Type			
Brush Type	**Does it pattern?**	**Patterning Mechanism**	**Evidence and Conclusions**
Unreinforced (Pre-patterning)	Yes	HA synthase function disrupted by ROS	Conclusion: • Patterning mechanism must be independent of HA.
Unreinforced (Post-patterning)	Yes	HA synthase function disrupted by ROS	Evidence: • Similar results from pre- and post-patterning suggest same mechanism. Conclusions: • HA-light interactions are minimal. • HA-ROS interactions are minimal.
Reinforced	Yes	HA-PEI amide bonds cleaved by ROS	Evidence: • Amide bonds are susceptible to ROS.
SDS-Treated Reinforced	No	None	Conclusions: • ROS are generated from fragments. • HA-light interactions are minimal. • PEI/GA-light interactions are minimal.

whether ROS, generated by photointeractions with the samples, might be involved. It is well-known that UV-irradiation can directly denature enzymes,[47] but our patterning scheme works well into the visible spectrum. Proteins cannot be damaged by visible light unless they contain side groups that are capable of absorbing those wavelengths, like flavins in flavoproteins.[48] However, visible light can indirectly damage proteins through the production of ROS resulting from the light's interaction with cellular components. The resulting ROS can, in turn, cleave peptide bonds[48−50] as well as drive lipid peroxidation.[51−53]

We increased levels of the antioxidant dithiothreitol (DTT) to sequester ROS and block its presumed role in brush patterning.[54,55] The results are revealing (Figure 6c,d). Increasing DTT significantly (50 mM) reduces the patterning efficacy, such that under conditions that would normally prevent brush growth in standard growth buffer (w/5 mM DTT) (Figure 6c), a substantial brush is still able to grow (Figure 6d). We then verified that for reinforced brushes, high DTT (50 mM) also significantly reduces the photopatterning efficacy (Figure 6e and Figure S3). Together these results confirm that ROS plays a crucial role in the photopatterning mechanism.

Although some ROS species have been shown to degrade HA,[56,57] the agreement between pre- and postpatterning results (Figure 4) indicates that direct ROS degradation of HA during postpatterning is not a dominant mechanism behind the change in brush height. Additionally, HA has been shown to not absorb visible light wavelengths, so it is unlikely that HA−light interactions play a role.[58,59] We therefore hypothesize that during prepatterning and postpatterning of *unreinforced brushes*, the ROS directly interacts with HA synthase through the cleavage of peptide bonds and/or with the surrounding lipids, destabilizing the local membrane and disrupting the transmembrane HA synthase.[42] As HA synthase enzyme structures are destabilized, their function can be lost, decreasing the fraction of active enzymes on the surface able to produce and/or stably anchor HA. The agreement between pre- and postpatterning (Figure 4 and Figure S2) strongly supports the conclusion that the enzyme activity is destroyed rather than altered. We can thus draw a particularly important conclusion: Photopatterning HA synthase-generated HA brushes with visible light enables the local tuning of the grafting density of the HA brush for both prepatterned and postpatterned unreinforced brushes *via* ROS destruction of HA synthase function.

What is the origin of the ROS? Since we have established that the photopatterning works even in the absence of HA (during prepatterning), we therefore hypothesized that the ROS originates from light−surface interactions rather than light−HA interactions. ROS generated from light−surface interactions could arise either from photochemistry with molecules in the protein and lipid-rich membrane fragments or from reactions with the underlying polyethylenimine-glutaraldehyde (PEI-GA) film used to bind the fragments to the substrate. To distinguish between these two possibilities, we attempted to pattern reinforced brushes with a reduced fragment presence through treatment with SDS to remove the membrane fragments.[40] The patterning failed at high and low DTT concentrations (see Figure 6e), with the initial brush height remaining unchanged at both DTT concentrations. This provides compelling evidence that light interactions with the membrane fragments are the likely source of ROS production. It also provides further evidence that photon−HA interactions and photon−PEI/GA interactions are not significant enough to detectably alter brush height.

The last puzzle in this story is the mechanism of the postpatterning of reinforced brushes. We have established that HA synthase plays no final role in these brushes, that the membrane fragments are necessary to generate ROS for patterning to work, and that ROS interactions with HA polymers are negligible. This led us to consider the vulnerability of the HA linkages (amide bonds) to the underlying substrate. We hypothesize that just like the peptide bonds in HA synthase, which are in fact a type of amide bond between amino acids, these amide bonds are disrupted by the ROS, which damages the HA anchoring to the surface. As these bonds are broken, the HA strands are lost from the brush and the height decreases.

https://dx.doi.org/10.1021/acsnano.0c06882
ACS Nano 2021, 15, 4268−4276

CONCLUSIONS AND FUTURE WORK

Table 1 summarizes the insights collected from integrating the results from the three photopatterning strategies used here on unreinforced (pre/post-) and reinforced brushes (postpatterning). Overall, the strategy to use visible light, in particular 405 nm, is effective in locally tuning brush height, creating sculpted topographies, and is amenable to different types of patterning and brushes. Using longer wavelengths is also possible, but requires higher energy densities (higher power and/or more exposure time) to achieve the same patterning results. In our lab, the maximum power available for the green and red lasers on the confocal microscope made patterning prohibitively time-consuming; however, stronger light sources would circumvent this limitation.

Expanding to mask-dependent photopatterning will facilitate rapid tailoring of the polymer brushes on much larger scales. Access to larger patterned areas will also enable atomic force microscope measurements of the dry brush height in order to verify our conclusion that photopatterning of the brush topography results from direct manipulation of the HA grafting density. Future studies comparing theoretical predictions of the shape and concentration profiles of patterned polymer brushes with the very evident splay observed in these studies (Figure 2b) are of interest and, moreover, will be crucial to help develop design rules for integrating expected splay into engineered brush topographies.

Our introduction of a versatile but simple method to sculpt ultrathick structured polymer brushes expands the horizon of an already rich arena of applications. Further, the results showcase the potential for leveraging nature's biological machines in designing extraordinary functional materials. The main advantage in this system arises from the order of magnitude increase in brush height, which provides more substrate/volume for interactions, access to more complex topographies, and direct visual characterization of the brush. Although the method is currently limited to enzyme-fabricated HA brushes, the biopolymer can be postmodified to manipulate its chemical identity for diversification of its scope of applications.[60−62] Ultimately, the ROS-photopatterning method introduced here might be extended to a growing class of enzyme-derived polymer brushes and films, which already include DNA[39] and polyhydroxyalkanoate (PHA)[38] materials made by the enzymes deoxynucleotidyl transferase and PHA synthase, and may include future materials made by untapped enzymes such as cellulose synthase.[63]

METHODS AND MATERIALS

Hyaluronan Synthase Bacterial Fragment Deposition on Surfaces. Coverslips (VWR 48366 246 or VWR 48366 067) were sonicated in ultrapure water and acetone and then rinsed in ultrapure water, dried with nitrogen, and plasma treated (Harrick Plasma, PDC-32G, high RF power, air, 1 min). Poly(ethyleneimine) (PEI) (Sigma 482595, average M_w 1.3 kDa, 50% w/v in H_2O) was diluted with ultrapure water to 2.5%, and using HCl, the pH adjusted to 7.0. The coverslips were allowed to incubate for 1 h with PEI, were rinsed and dried, and then incubated with 2.5% glutaraldehyde (Sigma G7651, average M_w 0.1 kDa, 50% w/v in H_2O, diluted with PBS). The top 0.8 mm of a 1−200 μL pipet tip (VWR 89079- 474) was placed on the PEI-GA side of the coverslip and sealed with vacuum grease (Dow Corning, high-vacuum grease). HA synthase-rich bacterial membrane fragments (30 μL of 0.2 mg/mL, diluted from 1 mg/mL in phosphate buffer) were added and incubated for 1 h. This solution was exchanged for a Tris storage buffer (pH 7.3, 50 mM Tris (BDH 0312), 500 mM NaCl, 20 mM DTT, 5% glycerol (Invitrogen LS15514011)), and samples were stored at −20 °C. A more detailed description is available in Wei *et al.*[40]

Hyaluronan Brush Growth. The Tris storage buffer was exchanged with a HA growth buffer (pH 7.3, 75 mM $NaKPO_4$, 50 mM NaCl, 20 mM $MgCl_2$, 0.1 mM EDTA, 5 mM DTT). After warming the sample, 5 mM each of uridine 5-diphosphoglucuronic acid trisodium salt (UDP-GlcUA, Sigma-Aldrich U6751) and uridine 5-diphospho-*N*-acetylglucosamine sodium salt (UDP-GlcNAc, Sigma-Aldrich U4375) were added to the growth buffer. The sample was incubated at 30 °C for the desired growth time. To halt HA synthesis, the activation buffer was gently removed by pipetting. 100 μL of a quenching wash (300 mM NaCl, 20 mM EDTA) was added, and the pipet mixed once and left to sit for 1 min. This solution was then removed from the sample, and 100 μL of the quenching wash was added, mixed, and allowed to sit for 1 min. After 1 min, the quenching wash was removed and replaced with 100 μL of 150 mM NaCl, and pipet was mixed once and removed. This was repeated once more. Finally, all of the NaCl solution was removed, and the imaging solution (see HA Brush Imaging below) was added, and the pipet was mixed gently three times.

Imaging the Hyaluronan Brush. Particle exclusion assays were performed using 0.7% w/v red, 200 nm latex FluoSpheres (carboxylate-modified Molecular Probes, Inc., F8810), 33 μg/mL of fluorescent dextran (Molecular Probes, Inc. Alexa Fluor 647, M_w 10 kDa), and 0.007% w/v of the green, 20 nm Fluospheres (catalog number: F8787).[43,44] We have established previously that 200 nm beads and larger remain excluded from the brush region. Therefore, using image analysis of confocal images to extract the location of the edge of the 200 nm beads allows for estimating of brush height. The smaller 20 nm beads penetrate the brush and stick to the underlying coverslip, providing a marker for the base of the brush. Images of the brush and beads were acquired using a scanning laser confocal microscope (FV1000, Olympus, Tokyo, Japan; objective: PlanApo N, 60×/1.42 NA oil). To image, a *z*-stack was created by taking 500 nm vertical *z*-steps over a total distance of 20 μm. Imaging was completed within 1 h after halting HA synthesis in order to avoid significant desorption of the HA polymers. Error bars in plots report the propagation of the standard deviation of measurements with the systemic error in the axial resolution of the confocal microscope (see Supporting Information). A more detailed description of height analysis and its validation is described in Wei *et al.*[40]

For height analysis of the squares in Figure 2, we measured the central portion of the 17.4 × 17.4 μm^2 squares (13.8 × 13.8 μm^2), eliminating data from the edges where the polymer splay distorts the results of the patterning. For height analysis of the gradient, the final brush height in each area was determined by the eye (rather than the quantitative image analysis used for other experiments) due to the very small areas sampled.

Optimizing Patterning Settings. A resolution of 512 × 512 pixels was always used. For each wavelength, the number of times the desired region was scanned (aka, the necessary exposure time) by the confocal microscope was varied. The minimum number of scan times necessary for brush elimination was determined using each laser set to 100% intensity. For λ = 405 nm, $P_{max,405}$ = 561 μW, the number of scans necessary was 5. For λ = 488 nm, $P_{max,488}$ = 458 μW, the number of scans necessary was 9. For λ = 635 nm, $P_{max,635}$ = 548 μW, the number of scans necessary was 60. For λ = 405 nm, the pinhole size is automatically determined by the software to be 85 μm. The axial resolution for λ = 405 nm is calculated according to the Supporting Information to be 426.9 nm. Once the number of scans was determined, this value would be set for all future experiments with that wavelength, and only the intensity of the laser would be varied between 0 and 100%. To determine how the number of scans and laser intensity translated to an applied energy density, measurement of the laser power at the objective was measured using a Coherent PowerMax-USB sensor (type 5499G16R) or a ThorLabs S170C Microscope Slide Power Sensor. This measurement was taken once every 6 months. In between measurements, the maximum energy density necessary to eliminate the brush appeared to drift over time, so the power rating of each laser according to the microscope software

https://dx.doi.org/10.1021/acsnano.0c06882
ACS Nano 2021, 15, 4268−4276

was used to calibrate for this drift which likely arose from slow deterioration of alignment. A description of the energy density calculation based on patterning parameters is provided in the Supporting Information.

Prepatterning (Binary/Variable/Gradient). After exchanging the Tris storage media for growth buffer, the sample was placed in a stage-top incubator at 30 °C with wet sponges to maintain humidity. A low concentration of 8 μm silica microspheres (Cospheric, SiO2MS-1.8 7.75um) were added and brought into focus with bright-field microscopy. The focus was adjusted by an amount equal to the radius below the center such that the focus should now be on the surface of the sample—at the plane of the membrane fragments. (Figure S1 shows that slight error in this focusing method of a few microns does not result in significantly different resulting brush heights.) The area of interest was chosen by setting the zoom factor (for square areas) or by setting the zoom factor for the area width and extending one side length to create a rectangle (such as for creating the gradient, where the area of the rectangle always matched that of the square area used for calibration). A resolution of 512 × 512 pixels was always used. The microscope's 405 nm laser raster (line) scanned the area using optimized settings. To apply the laser to a new area, we refocused on the fragment surface using the microspheres and then proceeded with the same steps as before. After all desired areas were laser treated, we activated the HA synthesis, and the sample grew for the desired time.

Chemical Reinforcement of HA to Substrate. At the end of HA synthesis, the growth solution was exchanged with an intermediate buffer of pH 7.0, 75 mM $NaKPO_4$, 50 mM NaCl three times. This solution was completely removed from the sample, and 100 mM 1-ethyl-3-(3-dimethylaminopropyl)carbodiimide (EDC, Sigma E1769) and 50 mM sulfo-*N*-hydroxysuccinimide (sulfo-NHS, Sigma-Aldrich 56485) (both in a solution of ultrapure water) were added to the sample and allowed to sit for 30 min. Afterward, the solution was exchanged with the same concentrations of newly dissolved EDC and sulfo-NHS, and the incubation was repeated. After a third repeat of the EDC/sulfo-NHS addition, the sample was left overnight at room temperature. The next day, if the sample was to be used right away, it was washed with 150 mM NaCl four times. If it was not to be used right away, then it was washed with a storage solution of 0.1 M glycine (OmniPur 4810) and 1% NaN_3 (Alfa Aesar 14314) and stored in a 4 °C fridge until later use. A more detailed description is previously described in Wei *et al.*[40]

Postpatterning (Unreinforced and Reinforced Brushes). For unreinforced brushes, after HA synthesis is halted, the solution on the sample is removed and replaced with the imaging solution. For reinforced brushes, after reinforcement, the sample is washed with 150 mM NaCl four times. This solution is then replaced with the imaging solution. The green, 20 nm nanoparticles stick to the PEI-GA layer on the glass interface which makes focusing on the fragment layer straightforward and avoids the use of the 8 μm silica microspheres. Once the focal plane is set, patterning can proceed as previously described: Setting the size of the area of interest with the zoom settings, defining the laser intensity or number of scans to set the energy density applied to the surface, allowing the laser to scan the area, refocusing for each new area, and repeating until all desired areas have been treated. Imaging can then proceed as normal since all the appropriate nanoparticles are already present on the sample.

SDS Treatment of Reinforced Brushes. After reinforcement, the sample was washed six times with a 20 mg/mL solution of sodium dodecyl sulfate (SDS, Sigma-Aldrich L6026) and allowed to sit for 30−60 min. The solution was then exchanged with 150 mM NaCl four times. The NaCl solution was then swapped for the imaging solution. A more detailed description is given in Wei *et al.*[40]

Comparing High and Low DTT Concentration Effects on Patterning. The growth buffer was used for low DTT concentration experiments (pH 7.3, 75 mM $NaKPO_4$, 50 mM NaCl, 20 mM $MgCl_2$, 0.1 mM EDTA, 5 mM DTT). For high DTT concentration experiments, the molarity was increased 10× to 50 mM DTT, while all other components remained unchanged. Patterning of each brush time proceeded according to their previously described protocols, where the brush was first patterned in the presence of the low DTT growth buffer. Then, after patterning was completed, the solution was exchanged three times for the high DTT growth buffer. The patterning was repeated, and the results compared.

Impact of Laser Focus Height above Surface during Patterning. We investigated the impact of the uncertainty of the laser focus on the patterning outcome since the center of the 8 μm silica microspheres is determined by the eye. We patterned different regions using several different focal planes above the presumed glass interface. To achieve this, the microspheres were brought into focus (at their expected center and widest point). The focus was adjusted by remotely moving the stage position varying amounts (0, 1, 2, 3, and 4 μm) in different patterned regions below the bead center such that the focus will be different heights above the glass interface. The same patterning settings were used in each scenario, and the resulting brush heights of each area were extracted. No significant dependence on the position of the focal plane was found (see Figure S1).

ASSOCIATED CONTENT

Supporting Information

The Supporting Information is available free of charge at https://pubs.acs.org/doi/10.1021/acsnano.0c06882.

Calculation of energy density, calculation of error for brush height measurements, calculation of confocal volume. Supplementary figures for patterning at different depths, pre-/postpatterning, and variable DTT experiment (PDF)

AUTHOR INFORMATION

Corresponding Author

Jennifer E. Curtis − *School of Physics, Georgia Institute of Technology, Atlanta, Georgia 30332, United States; Parker H. Petit Institute for Bioengineering and Biosciences, Atlanta, Georgia 30332, United States;* orcid.org/0000-0001-5460-756X; Email: jennifer.curtis@physics.gatech.edu

Authors

Jessica L. Faubel − *School of Physics, Georgia Institute of Technology, Atlanta, Georgia 30332, United States*

Wenbin Wei − *School of Physics, Georgia Institute of Technology, Atlanta, Georgia 30332, United States*

Complete contact information is available at: https://pubs.acs.org/10.1021/acsnano.0c06882

Author Contributions

J.L.F. was responsible for research design, experimentation, data interpretation, and manuscript preparation. W.W. was responsible for concept and research design. J.E.C. was responsible for concept and research design, data interpretation, supervision, and manuscript preparation. All authors read and approved the final manuscript.

Notes

The authors declare no competing financial interest.

ACKNOWLEDGMENTS

We are grateful to B. Brettmann for helpful insights. We thank P. H. Weigel and J. L. Washburn for their help with the hyaluronan synthase-rich bacterial membrane fragments and many useful discussions. Additionally, we gratefully acknowledge funding support from the NSF DMR, grant nos. 0955811 and 1709897.

https://dx.doi.org/10.1021/acsnano.0c06882
ACS Nano 2021, 15, 4268−4276

REFERENCES

(1) Xie, Z.; Gan, T.; Fang, L.; Zhou, X. Recent Progress in Creating Complex and Multiplexed Surface-Grafted Macromolecular Architectures. *Soft Matter* **2020**, *16*, 8736−8759.

(2) Zhou, X.; Liu, X.; Xie, Z.; Zheng, Z. 3D-Patterned Polymer Brush Surfaces. *Nanoscale* **2011**, *3*, 4929−4939.

(3) Benetti, E. M. Quasi-3D-Structured Interfaces by Polymer Brushes. *Macromol. Rapid Commun.* **2018**, *39*, 1800189.

(4) Bhat, R. R.; Tomlinson, M. R.; Wu, T.; Genzer, J. Surface-Grafted Polymer Gradients: Formation, Characterization, and Applications. In *Surface-Initiated Polymerization II*; Jordan, R., Ed. Springer: Berlin, Heidelberg, 2006; pp 51−124.

(5) Genzer, J. Surface-Bound Gradients for Studies of Soft Materials Behavior. *Annu. Rev. Mater. Res.* **2012**, *42*, 435−468.

(6) Genzer, J.; Bhat, R. R. Surface-Bound Soft Matter Gradients. *Langmuir* **2008**, *24*, 2294−2317.

(7) Bhat, R. R.; Genzer, J. Combinatorial Study of Nanoparticle Dispersion in Surface-Grafted Macromolecular Gradients. *Appl. Surf. Sci.* **2006**, *252*, 2549−2554.

(8) Xu, C.; Wu, T.; Drain, C. M.; Batteas, J. D.; Fasolka, M. J.; Beers, K. L. Effect of Block Length on Solvent Response of Block Copolymer Brushes: Combinatorial Study with Block Copolymer Brush Gradients. *Macromolecules* **2006**, *39*, 3359−3364.

(9) Wu, T.; Efimenko, K.; Genzer, J. Combinatorial Study of the Mushroom-to-Brush Crossover in Surface Anchored Polyacrylamide. *J. Am. Chem. Soc.* **2002**, *124*, 9394−9395.

(10) Wu, T.; Gong, P.; Szleifer, I.; Vlcek, P.; Subr, V.; Genzer, J. Behavior of Surface-Anchored Poly(Acrylic Acid) Brushes with Grafting Density Gradients on Solid Substrates: 1. Experiment. *Macromolecules* **2007**, *40*, 8756−8764.

(11) Zhao, B. A Combinatorial Approach to Study Solvent-Induced Self-Assembly of Mixed Poly(Methyl Methacrylate)/Polystyrene Brushes on Planar Silica Substrates: Effect of Relative Grafting Density. *Langmuir* **2004**, *20*, 11748−11755.

(12) Bhat, R. R.; Tomlinson, M. R.; Genzer, J. Orthogonal Surface-Grafted Polymer Gradients: A Versatile Combinatorial Platform. *J. Polym. Sci., Part B: Polym. Phys.* **2005**, *43*, 3384−3394.

(13) Chen, T.; Chang, D. P.; Zhang, J.; Jordan, R.; Zauscher, S. Manipulating the Motion of Gold Aggregates Using Stimulus-Responsive Patterned Polymer Brushes as a Motor. *Adv. Funct. Mater.* **2012**, *22*, 429−434.

(14) Ren, T.; Mao, Z.; Guo, J.; Gao, C. Directional Migration of Vascular Smooth Muscle Cells Guided by a Molecule Weight Gradient of Poly(2-Hydroxyethyl Methacrylate) Brushes. *Langmuir* **2013**, *29*, 6386−6395.

(15) Benetti, E. M.; Gunnewiek, M. K.; van Blitterswijk, C. A.; Julius Vancso, G.; Moroni, L. Mimicking Natural Cell Environments: Design, Fabrication and Application of Bio-Chemical Gradients on Polymeric Biomaterial Substrates. *J. Mater. Chem. B* **2016**, *4*, 4244−4257.

(16) Mei, Y.; Wu, T.; Xu, C.; Langenbach, K. J.; Elliott, J. T.; Vogt, B. D.; Beers, K. L.; Amis, E. J.; Washburn, N. R. Tuning Cell Adhesion on Gradient Poly(2-Hydroxyethylmethacrylate)-Grafted Surfaces. *Langmuir* **2005**, *21*, 12309−12314.

(17) Ionov, L.; Houbenov, N.; Sidorenko, A.; Stamm, M.; Luzinov, I.; Minko, S. Inverse and Reversible Switching Gradient Surfaces from Mixed Polyelectrolyte Brushes. *Langmuir* **2004**, *20*, 9916−9919.

(18) Oh, S. H.; Kim, T. H.; Im, G. I.; Lee, J. H. Investigation of Pore Size Effect on Chondrogenic Differentiation of Adipose Stem Cells Using a Pore Size Gradient Scaffold. *Biomacromolecules* **2010**, *11*, 1948−1955.

(19) Bhat, R. R.; Genzer, J.; Chaney, B. N.; Sugg, H. W.; Liebmann-Vinson, A. Controlling the Assembly of Nanoparticles Using Surface Grafted Molecular and Macromolecular Gradients. *Nanotechnology* **2003**, *14*, 1145−1152.

(20) Bhat, R. R.; Tomlinson, M. R.; Genzer, J. Assembly of Nanoparticles Using Surface-Grafted Orthogonal Polymer Gradients. *Macromol. Rapid Commun.* **2004**, *25*, 270−274.

(21) Luzinov, I.; Minko, S.; Tsukruk, V. V. Responsive Brush Layers: From Tailored Gradients to Reversibly Assembled Nanoparticles. *Soft Matter* **2008**, *4*, 714.

(22) Wang, X.; Tu, H.; Braun, P. V.; Bohn, P. W. Length Scale Heterogeneity in Lateral Gradients of Poly(N-Isopropylacrylamide) Polymer Brushes Prepared by Surface-Initiated Atom Transfer Radical Polymerization Coupled with In-Plane Electrochemical Potential Gradients. *Langmuir* **2006**, *22*, 817−823.

(23) Schuh, C.; Santer, S.; Prucker, O.; Rühe, J. Polymer Brushes with Nanometer-Scale Gradients. *Adv. Mater.* **2009**, *21*, 4706−4710.

(24) Chen, T.; Jordan, R.; Zauscher, S. Dynamic Microcontact Printing for Patterning Polymer-Brush Microstructures. *Small* **2011**, *7*, 2148−2152.

(25) Liu, X.; Li, Y.; Zheng, Z. Programming Nanostructures of Polymer Brushes by Dip-Pen Nanodisplacement Lithography (Dnl). *Nanoscale* **2010**, *2*, 2614−2618.

(26) Steenackers, M.; Jordan, R.; Küller, A.; Grunze, M. Engineered Polymer Brushes by Carbon Templating. *Adv. Mater.* **2009**, *21*, 2921−2925.

(27) Higashi, J.; Nakayama, Y.; Marchant, R. E.; Matsuda, T. High-Spatioresolved Microarchitectural Surface Prepared by Photograft Copolymerization Using Dithiocarbamate: Surface Preparation and Cellular Responses. *Langmuir* **1999**, *15*, 2080−2088.

(28) Liu, X.; Guo, S.; Mirkin, C. A. Surface and Site-Specific Ring-Opening Metathesis Polymerization Initiated by Dip-Pen Nanolithography. *Angew. Chem.* **2003**, *115*, 4933−4937.

(29) Harris, B. P.; Metters, A. T. Generation and Characterization of Photopolymerized Polymer Brush Gradients. *Macromolecules* **2006**, *39*, 2764−2772.

(30) Chen, T.; Amin, I.; Jordan, R. Patterned Polymer Brushes. *Chem. Soc. Rev.* **2012**, *41*, 3280−3296.

(31) Barbey, R.; Lavanant, L.; Paripovic, D.; Schuwer, N.; Sugnaux, C.; Tugulu, S.; Klok, H.-A. Polymer Brushes *Via* Surface-Initiated Controlled Radical Polymerization: Synthesis, Characterization, Properties, and Applications. *Chem. Rev.* **2009**, *109*, 5437−5527.

(32) Zhang, J.; Han, Y. Active and Responsive Polymer Surfaces. *Chem. Soc. Rev.* **2010**, *39*, 676−693.

(33) Ducker, R.; Garcia, A.; Zhang, J.; Chen, T.; Zauscher, S. Polymeric and Biomacromolecular Brush Nanostructures: Progress in Synthesis, Patterning and Characterization. *Soft Matter* **2008**, *4*, 1774−1786.

(34) Lin, X.; He, Q.; Li, J. Complex Polymer Brush Gradients Based on Nanolithography and Surface-Initiated Polymerization. *Chem. Soc. Rev.* **2012**, *41*, 3584−3593.

(35) Zhou, X.; Wang, X.; Shen, Y.; Xie, Z.; Zheng, Z. Fabrication of Arbitrary Three-Dimensional Polymer Structures by Rational Control of the Spacing between Nanobrushes. *Angew. Chem., Int. Ed.* **2011**, *50*, 6506−6510.

(36) Ulbricht, M.; Yang, H. Porous Polypropylene Membranes with Different Carboxyl Polymer Brush Layers for Reversible Protein Binding *Via* Surface-Initiated Graft Copolymerization. *Chem. Mater.* **2005**, *17*, 2622−2631.

(37) Saito, K. Charged Polymer Brush Grafted onto Porous Hollow-Fiber Membrane Improves Separation and Reaction in Biotechnology. *Sep. Sci. Technol.* **2002**, *37*, 535−554.

(38) Kim, Y.-R.; Paik, H.-J.; Ober, C. K.; Coates, G. W.; Batt, C. A. Enzymatic Surface-Initiated Polymerization: A Novel Approach for the *in Situ* Solid-Phase Synthesis of Biocompatible Polymer Poly(3-Hydroxybutyrate). *Biomacromolecules* **2004**, *5*, 889−894.

(39) Barbee, K. D.; Chandrangsu, M.; Huang, X. Fabrication of DNA Polymer Brush Arrays by Destructive Micropatterning and Rolling-Circle Amplification. *Macromol. Biosci.* **2011**, *11*, 607−617.

(40) Wei, W.; Faubel, J. L.; Selvakumar, H.; Kovari, D. T.; Tsao, J.; Rivas, F.; Mohabir, A. T.; Krecker, M.; Rahbar, E.; Hall, A. R.; Filler, M. A.; Washburn, J. L.; Weigel, P. H.; Curtis, J. E. Self-Regenerating Giant Hyaluronan Polymer Brushes. *Nat. Commun.* **2019**, *10*, 5527.

(41) Faubel, J. L.; Patel, R. P.; Wei, W.; Curtis, J. E.; Brettmann, B. K. Giant Hyaluronan Polymer Brushes Display Polyelectrolyte Brush Polymer Physics Behavior. *ACS Macro Lett.* **2019**, *8*, 1323−1327.

https://dx.doi.org/10.1021/acsnano.0c06882
ACS Nano 2021, 15, 4268−4276

(42) Tlapak-Simmons, V. L.; Baggenstoss, B. A.; Clyne, T.; Weigel, P. H. Purification and Lipid Dependence of the Recombinant Hyaluronan Synthases from *Streptococcus Pyogenes* and *Streptococcus Equisimilis*. *J. Biol. Chem.* **1999**, *274*, 4239−4245.
(43) McLane, L. T.; Chang, P.; Granqvist, A.; Boehm, H.; Kramer, A.; Scrimgeour, J.; Curtis, J. E. Spatial Organization and Mechanical Properties of the Pericellular Matrix on Chondrocytes. *Biophys. J.* **2013**, *104*, 986−996.
(44) Chang, P. S.; McLane, L. T.; Fogg, R.; Scrimgeour, J.; Temenoff, J. S.; Granqvist, A.; Curtis, J. E. Cell Surface Access Is Modulated by Tethered Bottlebrush Proteoglycans. *Biophys. J.* **2016**, *110*, 2739−2750.
(45) Mathieu, M.; Friebe, A.; Franzka, S.; Ulbricht, M.; Hartmann, N. Surface-Initiated Polymerization on Laser-Patterned Templates: Morphological Scaling of Nanoconfined Polymer Brushes. *Langmuir* **2009**, *25*, 12393−12398.
(46) Lee, W. K.; Patra, M.; Linse, P.; Zauscher, S. Scaling Behavior of Nanopatterned Polymer Brushes. *Small* **2007**, *3*, 63−66.
(47) Neurath, H.; Greenstein, J. P.; Putnam, F. W.; Erickson, J. A. The Chemistry of Protein Denaturation. *Chem. Rev.* **1944**, *34*, 157−265.
(48) Lavi, R.; Shainberg, A.; Shneyvays, V.; Hochauser, E.; Isaac, A.; Zinman, T.; Friedmann, H.; Lubart, R. Detailed Analysis of Reactive Oxygen Species Induced by Visible Light in Various Cell Types. *Lasers Surg. Med.* **2010**, *42*, 473−480.
(49) de Jager, T. L.; Cockrell, A. E.; Du Plessis, S. S. Ultraviolet Light Induced Generation of Reactive Oxygen Species. In *Ultraviolet Light in Human Health, Diseases and Environment*; Ahmad, S. I., Ed.; Springer International Publishing: Cham, 2017; pp 15−23.
(50) Gracy, R. W.; Talent, J. M.; Kong, Y.; Conrad, C. C. Reactive Oxygen Species: The Unavoidable Environmental Insult? *Mutat. Res., Fundam. Mol. Mech. Mutagen.* **1999**, *428*, 17−22.
(51) Hayyan, M.; Hashim, M. A.; AlNashef, I. M. Superoxide Ion: Generation and Chemical Implications. *Chem. Rev.* **2016**, *116*, 3029−3085.
(52) Araki, T.; Kitaoka, H. The Mechanism of Reaction of Ebselen with Superoxide in Aprotic Solvents as Examined by Cyclic Voltammetry and Esr. *Chem. Pharm. Bull.* **2001**, *49*, 541−545.
(53) Li, R.; Guiney, L. M.; Chang, C. H.; Mansukhani, N. D.; Ji, Z.; Wang, X.; Liao, Y. P.; Jiang, W.; Sun, B.; Hersam, M. C.; Nel, A. E.; Xia, T. Surface Oxidation of Graphene Oxide Determines Membrane Damage, Lipid Peroxidation, and Cytotoxicity in Macrophages in a Pulmonary Toxicity Model. *ACS Nano* **2018**, *12*, 1390−1402.
(54) Maisin, J. R.; Mattelin, G. Reduction in Radiation Lethality by Mixtures of Chemical Protectors. *Nature* **1967**, *214*, 207−208.
(55) Bick, Y. A. E.; Jackson, W. D. Chemical Protection against X-Irradiation by a New Reducing Agent 1,4-Dithiothreitol in Marsupial Leucocytes in Culture. *Nature* **1968**, *217*, 479−480.
(56) Duan, J.; Kasper, D. L. Oxidative Depolymerization of Polysaccharides by Reactive Oxygen/Nitrogen Species. *Glycobiology* **2011**, *21*, 401−409.
(57) Soltes, L.; Mendichi, R.; Kogan, G.; Schiller, J.; Stankovska, M.; Arnhold, J. Degradative Action of Reactive Oxygen Species on Hyaluronan. *Biomacromolecules* **2006**, *7*, 659−668.
(58) Huang, Y. C.; Huang, K. Y.; Lew, W. Z.; Fan, K. H.; Chang, W. J.; Huang, H. M. Gamma-Irradiation-Prepared Low Molecular Weight Hyaluronic Acid Promotes Skin Wound Healing. *Polymers (Basel, Switz.)* **2019**, *11*, 1214.
(59) Hafsa, J.; Chaouch, M. A.; Charfeddine, B.; Rihouey, C.; Limem, K.; Le Cerf, D.; Rouatbi, S.; Majdoub, H. Effect of Ultrasonic Degradation of Hyaluronic Acid Extracted from Rooster Comb on Antioxidant and Antiglycation Activities. *Pharm. Biol.* **2017**, *55*, 156−163.
(60) Burdick, J. A.; Prestwich, G. D. Hyaluronic Acid Hydrogels for Biomedical Applications. *Adv. Mater.* **2011**, *23*, H41−56.
(61) Chow, D. C.; Lee, W.-K.; Zauscher, S.; Chilkoti, A. Enzymatic Fabrication of DNA Nanostructures: Extension of a Self-Assembled Oligonucleotide Monolayer on Gold Arrays. *J. Am. Chem. Soc.* **2005**, *127*, 14122−14123.
(62) Galvin, C. J.; Genzer, J. Applications of Surface-Grafted Macromolecules Derived from Post-Polymerization Modification Reactions. *Prog. Polym. Sci.* **2012**, *37*, 871−906.
(63) Klemm, D.; Schumann, D.; Udhardt, U.; Marsch, S. Bacterial Synthesized Cellulose - Artificial Blood Vessels for Microsurgery. *Prog. Polym. Sci.* **2001**, *26*, 1561−1603.

https://dx.doi.org/10.1021/acsnano.0c06882
ACS Nano 2021, 15, 4268−4276